Hydrodynamic Modeling on the External Liquid–Solid Wetting Efficiency in a Trickling Flow Reactor

Zhen-Min Cheng, Xiang-Ming Kong, Jun Zhu, Zhen-Yuan Wang, Jian Jin, and Zi-Bin Huang
State Key Laboratory of Chemical Engineering, East China University of Science and Technology, Shanghai 200237, P.R. China

DOI 10.1002/aic.13785
Published online March 27, 2012 in Wiley Online Library (wileyonlinelibrary.com).

A three-region model was proposed, which considers the bed cross section being composed of a stagnant liquid region, a liquid film region, and a rivulet flow region. To estimate the fractions of the three regions, the fraction of film flow was evaluated first, by transforming the complex trickling flow texture into pure liquid film flow. Through the measurements of liquid holdup and pressure drop for the film flow, a relationship between relative permeability and gas saturation was established, and from which the fraction of film flow region was obtained. It shows packing size is most important to the faction of rivulet flow. The external wetting efficiency of the packing was correlated as the sum of two-third power of the liquid film fraction and the rivulet flow fraction, besides, a correlation based on Reynolds and Galileo numbers of the two phases in the form of $\eta_{ce} = 4.85Re_L^{0.42}\ Ga_L^{-0.25}\ Re_G^{0.083}$ *was proposed.* © 2012 American Institute of Chemical Engineers *AIChE J,* 59: 283–294, 2013

Keywords: trickle-bed reactor, liquid flow texture, three-region model, liquid–solid wetting efficiency correlation

Introduction

The incomplete wetting of the catalyst has been a critical and common problem, which affects the efficiency and safety of a trickling flow reactor. In the past decades, the liquid–solid contacting efficiency has been estimated mostly in the indirect manners—the tracer technology[1–6] or the reaction rate method.[7,8] Although hydrodynamic method has been considered in some research, however, it was only defined as the ratio of the two shear stresses in two-phase and in liquid-phase flow, without evaluating the wetting condition of the bed[9] or directly correlated with the pressure drop and Reynolds number,[10] without knowing the real wetting condition of packing. Therefore, the understanding on liquid–solid contacting up to now is rather superficial, the external wetting efficiency is simply considered as a lumped function of the liquid physical property, the pellet geometry and diameter, the porosity of the reactor, and the liquid velocity. In this work, we believe that it is possible to estimate the external contacting efficiency *a priori* once the overall liquid flow texture could be determined quantitatively.

The flow texture is rather complex in the trickling flow reactor, for instance, Le Goff and his coworkers (see Ref. 49 in Hofmann, 1978)[11] assumed that the liquid can flow down the packing either in continuous films, in rivulets, or in droplets in terms of the ''film-rivulet-drop'' model. Besides, they determined the liquid texture by measuring the electrical conductance of the liquid parallel and perpendicular to the direction of flow, and depicted the fractions of film, rivulet, and droplet in the same figure. In a different approach based on computer-assisted tomography (CAT), Ng and Chu[12] considered the liquid is present in forms of films, pendular droplets, liquid pockets, and filaments. Although the liquid flow concept described above has now been extensively accepted, the quantitative investigation on the proportions of the different forms of liquid flow is inadequate.

Due to the importance of liquid flow texture to pressure drop, holdup, wetting efficiency, and other reactor parameters, a large amount of visualization techniques have developed to provide direct observation on the real liquid–solid contacting status. The first three-dimensional flow visualization using CAT in a trickle bed was reported by Lutran et al.[13] Although the experiments were taken under single phase flow of the liquid, the results are valuable for the study of two-phase flow in the trickling regime in view of the negligible interaction between the gas and the liquid. They studied the effect of packing size via 3- and 6-mm particles, the effect of prewetting on the flow texture, as well as the influence of liquid surface tension. They found that rivulet flow is three-dimensional rather than completely vertically downward, and its shape is varying because of splitting and coalescence. The particle size is important to the formation of rivulet flow, which showed significant rivulets in the 3-mm packing bed, whereas film flow was predominant in the 6-mm packing bed. Besides, prewetting of the packing plays a crucial role, because when the liquid flow rate was decreased in a prewetted bed, film flow instead of rivulet flow was observed primarily. With an improved voxel resolution over the bed cross section at $313 \times 313\ \mu m^2$ in two dimensions and $328 \times 328 \times 328\ \mu m^3$ in three dimensions provided by magnetic resonance imaging, Sederman and Gladden[14] measured the liquid holdup and wetting efficiency

Correspondence concerning this article should be addressed to Z.-M. Cheng at zmcheng@ecust.edu.cn.

distribution in the range of trickle flow for a packed bed of internal diameter 40 mm containing 5-mm diameter glass beads. They observed the number of rivulets increased from 0 to about 30 with the increase of liquid flow rate. Recently, a X-ray computed tomography with a higher spatial resolution of 118 μm pixel^{-1} was developed by van der Merwe et al.,[15] which could accurately identify the phase interfaces in an unbiased way in a trickle bed, where the dynamic liquid was shown both in film and rivulet, which are randomly distributed over the bed cross section.

Apart from these works, there are still many other investigations utilizing X-ray and γ-ray radiographies to monitor the liquid flow texture in the trickle bed. Although most of them are focused on the distribution of the liquid phase on the bed scale without discrimination between film and rivulet, it is still obvious to find evidence of the multiple liquid flow morphologies. For example, Marchot et al.[16,17] measured a strong increase of dynamic liquid holdup at the interface between packing elements in an experimental setup made of a 2-m high and 0.6-m internal diameter packed with corrugated sheet structured packing of Sulzer Mellapak by a self-designed X-ray tomograph that could rotate around a vertical axis to give scans of horizontal sections of the column. van der Merwe et al.[18] studied the multiple hydrodynamic states and the temporal stability of liquid distribution under different operation modes in a trickle bed packed with 2.5-mm alumina spheres by a cone beam X-ray radiography. To accurately characterize the gas–liquid flow distribution inside a large catalytic bed, γ-ray tomographic system has been developed because of its much higher radiation intensity than the X-ray.[19,20] As the column diameter is too large, it is not suitable to study the liquid morphology on the particle and pore scales.

In addition, dye adsorption has also been developed as a visualization technique in liquid flow characterization. Ravindra et al.[21] marked the particles by injection of methylene-blue solution. They observed the channel flow would split, merge, and split again in the downward flow process, and from the exit liquid collection device, they deduced that the channel flow is composed of a liquid filament with a periphery of film flow over the particles. In a more recent work, Baussaron et al.[22,23] combined particle image velocimetry (PIV) and dye-adsorption to detect the wetting structure inside a catalytic bed exposed to a gas–liquid trickling flow. From the velocity fields measured with PIV for the water–alumina system, three velocity zones were detected on the particle surface, and there was no completely motionless liquid being observed. In the dye-adsorption measurements, completely dry zones were observed in the absence of prewetting due to severe channel flow at low liquid velocities, however, this channeling could not be eliminated, unless the liquid flow is high enough to force new paths inside the bed. For a total wetting efficiency of 0.75, 45% of pellets were almost completely wetted. At the lowest liquid velocity, only 18% of the particles were completely wetted, whereas nearly 20% of the pellets were almost dry.

It is clear that the above experimental investigations have confirmed the existence of multiple liquid–solid contacting states. However, the prediction of this hydrodynamic phenomenon seems very difficult even with computational fluid dynamics (CFD). Despite there are a large amount of CFD publications on trickle bed study, most of the researches are only concerned with the prediction of pressure drop and liquid holdup, which employs the Eulerian–Eulerian two-fluid model.[24–29] As in the framework of the Eulerian model, the two phases are treated mathematically as interpenetrating continua, which means there is no interface between the gas and liquid. Owing to this limitation, Lopes and Quinta-Ferreira[30,31] applied the volume-of-fluid model, however, quantitative results on solid wetting and liquid flow texture are not yet obtained. The failure in CFD simulation may be due to different forms of liquid that are scattered randomly in the bed, and a clear discrimination between film and rivulet is difficult, recalling that CFD simulation is based on the Navier–Stokes equation, which is only concerned with the mass and momentum conservations. Therefore, due to the complex structure of porous medium in packed beds and the complexities involved with the interfacial interactions, it is hard to formulate appropriate boundary conditions for a quantitative description of two-phase flow through a packed bed on the basis of first principles.[32]

Theoretical Development

In the past decades, two approaches have been reported in the prediction of wetting efficiency and liquid distribution on the reactor scale. The first one was a statistical hydrodynamics establishment introduced by Crine et al.[33] In this method, the modeling of two-phase flow on the microscale in terms of the Ergun's equation was extended to the bed scale by defining local probability distribution of the Reynolds number according to the maximum entropy principle. As the local liquid holdup and wetting efficiency are available at each local Reynolds number, the overall values of the two parameters on the bed scale could be obtained through a weighted summation. However, the validity of this method depends on the correct definition of the minimum Reynolds number below which the catalyst is not wetted, and also on the Reynolds number distribution probability which determines the influence of liquid flow rate. Another approach was a parallel-zone model proposed by Wang et al.[34] In their work, the reactor bed was classified into a gas zone with no liquid flow, a liquid zone with no gas flow, and a two-phase flow zone. The three zones are considered working in parallel subjected to the same pressure drop of the reactor. Through solving the respective pressure-drop equations, the velocity in each zone and therefore the fraction of each zone could be determined. Although the concept of the parallel-zone model is correct in principle, its accuracy in velocity prediction is not guaranteed, as the coefficients in the Ergun equation for a dry, wetted, or with gas–liquid flow are much different.[35]

In this work, a new model will be established under balance conservation of liquid holdup over the bed cross section without calculation of the velocity in each zone. Three distinctive liquid–solid contacting regions in parallel are defined below:

1. *The stagnant liquid region:* the liquid is stagnant, and the only flowing phase is gas.

2. *The liquid film region:* the liquid is flowing over the packing as films, and the gas is flowing in the void space of the packing.

3. *The rivulet flow region:* the liquid phase is filling in the interstitials among the packings, and therefore the gas flow is excluded in this region.

The fractions of the three regions are denoted as Φ_{stag}, Φ_{film}, and Φ_{riv}. According to the definition, the film flow

fraction in the bed cross section could be expressed as a product of two terms

$$\Phi_{\text{film}} = \frac{\varepsilon_{\text{film,L}}}{\varepsilon_{\text{L}}} \cdot \frac{\varepsilon_{\text{L}}}{\varepsilon_{\text{L}}^*} \tag{1}$$

where the first term denotes the fraction of film flow with respect to the bed-scale dynamic liquid holdup, ε_{L}, which is obtained from the total liquid holdup measured by electrical capacity tomography (ECT) minus the static one; whereas the second term is a measure of the wetting fraction of the bed expressed as the ratio of two liquid holdups ε_{L} and ε_{L}^*, which are, respectively, measured under partial and complete wetting conditions of the trickle bed. Normally, ε_{L}^* is the dynamic liquid holdup at the pulsing flow inception point, at which the bed is completely wetted.

As the dynamic liquid holdup of the bed is composed of the contributions from liquid film and rivulet, it gives

$$\varepsilon_{\text{L}} = \varepsilon_{\text{film,L}} + \varepsilon_{\text{riv}} \tag{2}$$

where ε_{riv} refers to the liquid holdup of rivulet over the cross section of the reactor.

Similar to Eq. 1, the fraction of rivulet flow is written as

$$\Phi_{\text{riv}} = \frac{\varepsilon_{\text{L}} - \varepsilon_{\text{film,L}}}{\varepsilon_{\text{L}}} \cdot \frac{\varepsilon_{\text{L}}}{\varepsilon_{\text{L}}^*} \tag{3}$$

In view of the volumetric balance of the three regions, the fraction of stagnant liquid is therefore obtained

$$\Phi_{\text{stag}} = 1 - \Phi_{\text{film}} - \Phi_{\text{riv}} \tag{4}$$

It has been shown that trickle bed is characterized with multiplicity in hydrodynamics, which is exhibited as hysteresis in pressure drop. The larger pressure drop gradient in the liquid flow rate decreasing path was explained due to better wetting of the packing, as the liquid–solid contacting angle in the two manners of operation are different,[36] and it was also explained due to the transformation of rivulet flow into film flow.[37] The two explanations are consistent and have been verified by Lutran et al.[13] from X-ray tomography, who observed that when the liquid flow rate was decreased in a prewetted bed, film flow instead of rivulet flow was detected primarily. In this work, to transform the rivulet flow entirely into film flow, the liquid flow rate was increased first to pulsing flow and then decreased inversely.

Sáez and Carbonell[38] showed the measured dimensionless pressure drop ψ_{G} can be expressed as a function of the gas phase permeability coefficient k_{G} based on the Ergun equation

$$\psi_{\text{G}} = \frac{1}{k_{\text{G}}} \left\{ A \frac{\text{Re}_{\text{G}}^*}{\text{Ga}_{\text{G}}^*} + B \frac{\text{Re}_{\text{G}}^2}{\text{Ga}_{\text{G}}^*} \right\} \tag{5}$$

with $A = 180$ and $B = 1.8$.

In Eq. 5, ψ_{G} is written as

$$\psi_{\text{G}} = \frac{1}{\rho_{\text{G}} g} \left(-\frac{\Delta P_{\text{G}}}{\Delta Z} \right) \tag{6}$$

And k_{G} is defined to a power of the gas phase saturation S_{G}

Table 1. Packing Characteristics

Packing	Shape	d_{p} (mm)	ε_{b}
Glass bead	Spherical	1.9	0.36
Glass bead	Spherical	3.6	0.375
Glass bead	Spherical	5.2	0.38
Glass bead	Spherical	9.3	0.39

$$k_{\text{G}} = S_{\text{G}}^{4.80} \tag{7}$$

with

$$S_{\text{G}} = 1 - \frac{\varepsilon_{\text{L}} + \varepsilon_{\text{s}}}{\varepsilon_{\text{b}}} \tag{8}$$

For the sake of a better precision, a segmented correlation of k_{G} has been suggested[32,39]

$$k_{\text{G}} = 0.4 S_{\text{G}}^{3.6} \quad (S_{\text{G}} \le 0.64) \tag{9}$$

$$k_{\text{G}} = S_{\text{G}}^{5.5} \quad (S_{\text{G}} > 0.64) \tag{10}$$

However, these correlations are obtained in the trickling regime with complex flow texture, and accordingly, they cannot be used in the situation when only film flow is left, which should be determined in this work.

In general, the relationship between k_{G} and S_{G} can be written as a product of two terms

$$k_{\text{G}} = \alpha \cdot S_{\text{G}}^{\beta} \tag{11}$$

where

$$k_{\text{G}} = \frac{1}{\psi_{\text{G}}} \left\{ A \frac{\text{Re}_{\text{G}}^*}{\text{Ga}_{\text{G}}^*} + B \frac{\text{Re}_{\text{G}}^2}{\text{Ga}_{\text{G}}^*} \right\} \tag{12}$$

It is noticed from Eq. 11, as $k_{\text{G}} = 1$ when $S_{\text{G}} = 1$, which leads to $\alpha = 1$, therefore, a large deviation of α from 1 would suggest a poor physical meaning between k_{G} and S_{G}.

Experimental Work

The trickling flow reactor was made of a transparent Plexiglass column of 14 cm in inside diameter and was packed to a height of 1 m with solid glass beads of uniform diameter with their properties shown in Table 1. A liquid distributor was installed 10 cm above the packing surface, and air and deionized water were used as the gas–liquid fluids. The liquid holdup was detected by a twin-plane PTL300E-TP-G ECT system manufactured by the Process Tomography, England. It is composed of a PTL300E capacitance measurement unit with a 12-electrode sliding ECT sensor installed on the 15-cm outside diameter (OD) Plexiglass column, and a set of Tomoflow Flowan software was used for signal acquisition and image processing. The measurement resolution of the ECT probe was 4.375×4.375 mm^2 at an image acquisition speed of 100 frames s^{-1}. The pressure drop was measured online by a differential transducer at a frequency of 200 Hz with its probes installed at the column wall above and below the packing bed. The ECT system was calibrated with the drainage method, which was accomplished with two magnetic valves installed both at the entrance and at the exit of the reactor.

The experiments were conducted under prewetted conditions. Before each experiment, the bed was completely wetted

Table 2. Comparison of Static Liquid Holdup from ECT with Eq. 13

	ε_s		
d_p (mm)	Exp.	Cal.	Relative Error (%)
1.9	0.04994	0.04990	+0.0922
3.6	0.04979	0.04984	−0.1049
5.2	0.04955	0.04967	−0.2351
9.3	0.04856	0.04856	+0.0104

for 15 min under pulsing flow condition. After prewetting, the gas and liquid were stopped simultaneously and allowed for draining for 30 min before the experimental runs. In each run, the gas flow rate was kept constant, whereas the liquid flow rate was first varied in an increasing mode from 0 to pulsing flow and was then decreased to 0. The liquid holdup and pressure drop data were measured for all the four particle diameters at three fixed gas flow rates and 19 liquid flow rates.

Results and Discussion

The static liquid holdup

The static liquid holdup ε_s was measured by ECT in the following sequence. The bed was first wetted at high gas and liquid flow rates, it was then drained freely for 30 min, and the liquid remaining in the bed measured is the static liquid holdup.

To verify the validity of the measurement on static liquid holdup, in Table 2, we compared the data with the estimation by empirical correlation suggested by Sáez and Carbonell[38]

$$\varepsilon_s = \frac{1}{20 + 0.9\text{Eö}} \tag{13}$$

where

$$\text{Eö} = \frac{\rho_L g d_p^2 \varepsilon_b^2}{\sigma(1-\varepsilon_b)} \tag{14}$$

It is found that the relative error between measurement and prediction is within ±0.3%, which is accurate enough in this work.

Hysteresis in liquid holdup

The hysteresis of liquid holdup was measured for different particle diameters of 1.9, 3.6, 5.2, and 9.3 mm under three gas flow rates of 0.065, 0.130, and 0.195 kg m^{-2} s^{-1}, and the liquid flow rate was varied from 0 to 18.04 kg m^{-2} s^{-1} and then decreased inversely. As shown in Figure 1, in all the experimental runs, the liquid holdup increased with the liquid flow rate, however, the influence of gas flow rate was rather weak. The discrepancy in the two branches of liquid holdup is obvious at low liquid flow rates, which means much different wetting condition of the catalyst bed. Lower liquid holdup was measured in the liquid flow rate increasing path, which means that a poorer liquid–solid wetting condition is encountered than that in the flow rate decreasing branch. However, the discrepancy in liquid holdup disappeared at relatively large liquid flow rates where the wetting is thought to be complete. The multiplicity in liquid holdup was observed for particle diameters 1.9, 3.6, and 5.2 mm, but it was negligible for 9.3 mm. It should be noted that the difference in liquid holdup was not so pronounced as in pressure drop, which would be difficult to measure by the traditional draining method.

Hysteresis in pressure drop

The pressure drop gradient under the two operating modes shows a much difference. The $(-\Delta P/\Delta Z)$ profile in the liquid flow rate increasing mode was always lower than that in the decreasing mode, until pulsing flow was reached. In addition, the shapes of the two $(-\Delta P/\Delta Z)$ profiles are substantially different, that is, the upper one is close to a straight line, whereas the lower one is more complicated. This difference implies that in the liquid flow rate increasing branch, the liquid–solid contacting state will undergo a series of changes, that is, from a low interaction state to a high one and eventually to the fully developed pattern. On the contrary, in the

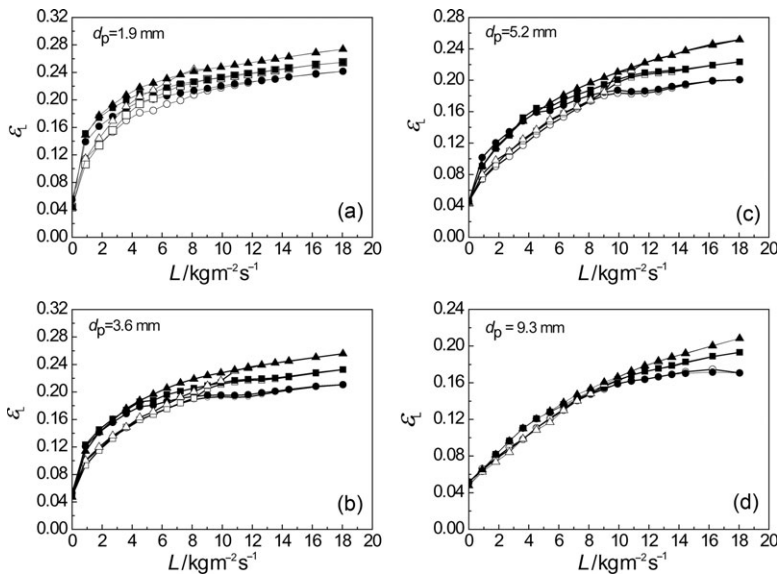

Figure 1. Liquid holdup measurements for different particle diameters.

Gas flow rate (kg m^{-2} s^{-1}): ○,●—0.065; □,■—0.130; △,▲—0.195; ○,□,△—liquid flow rate increasing; ●,■,▲—liquid flow rate decreasing. Packing diameters of (a) 1.9 mm, (b) 3.6 mm, (c) 5.2 mm, and (d) 9.3 mm.

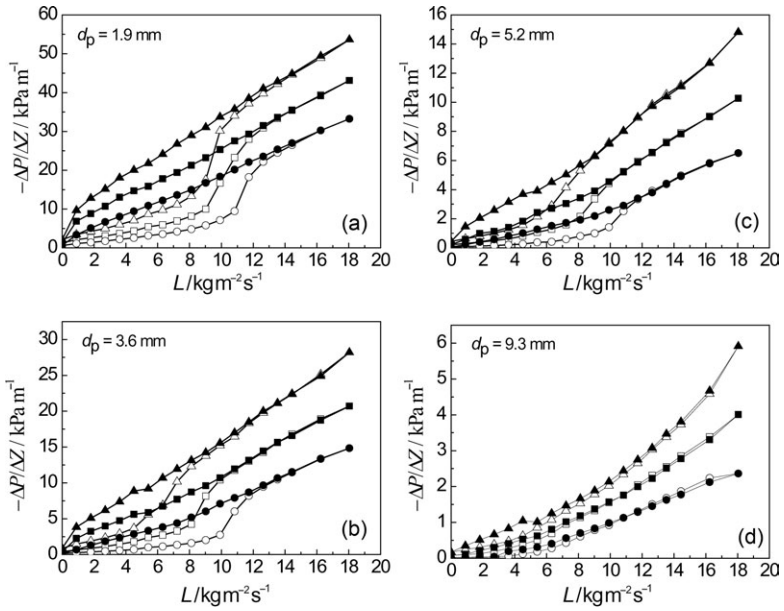

Figure 2. Influence of gas and liquid flow rates on the formation of pressure drop hysteresis loops.

Gas flow rate (kg m^{-2} s^{-1}): ○,●—0.065; □,■—0.130; △▲—0.195; ○,□,△—liquid flow rate increasing; ●,■,▲—liquid flow rate decreasing. Packing diameters of (a) 1.9 mm, (b) 3.6 mm, (c) 5.2 mm, and (d) 9.3 mm.

liquid flow rate decreasing branch, it seems the liquid–solid contacting state keeps constant, because pressure drop only linearly varies with the liquid flow rate. From the comparison on the profiles in Figures 2a–d, it shows the size of the pressure drop hysteresis loop decreases with the increase of particle size from 1.9 and 3.6 to 5.2 mm and eventually disappears at the largest particle size of 9.3 mm. In view of the particle size effect as reported by Lutran et al.,[13] who observed significant rivulets in the 3-mm packing bed although only film flow was predominant in the 6-mm packing bed, the decrease of pressure drop hysteresis loop with the increase of particle size is due to the reduction in the multiplicity in liquid–solid wetting condition that is determined by the content of film flow in the complex liquid flow texture.

Liquid flow texture characterization

In this paragraph, the wetting condition of the trickle bed will be characterized from the hysteresis in liquid holdup and pressure drop. It is known in the trickling flow regime, the solid is contacted with the liquid in three forms: the stagnant liquid, the liquid film, and the rivulet flow, however, it is not possible to estimate their fractions directly, while the following procedure is suggested to be followed.

Film Flow Property. According to Eq. 1, the film flow fraction can be obtained only if the liquid holdup in the film flow region is known. In view of the volumetric balance relation between the liquid holdup and gas holdup, it is required to evaluate the gas holdup in advance, which can be calculated from the gas phase saturation. As shown in Eq. 11, once the gas-phase relative permeability k_G is known, the gas phase saturation S_G will be determined. It is known k_G can be obtained directly from the experimental pressure drop according to Eq. 12, therefore, a relationship between k_G and S_G can be established.

In Table 3, the correlations between k_G and S_G are presented separately with respect to the two operation modes in liquid flow rate. It shows that the correlation coefficients in the runs of liquid flow rate decreasing branch are very close to 1.0, especially at gas velocities of 0.130 and 0.195 kg m^{-2} s^{-1}. In comparison, the coefficients in the runs of liquid flow rate increasing branch are all deviated from 1 remarkably.

When k_G is plotted against S_G in the two operation modes, as shown in Figure 3, the k_G vs. S_G profiles in the liquid flow rate decreasing branch are below those of the increasing branch, which means a lower gas phase permeability at the same liquid holdup. This result would indicate that in the liquid flow rate decreasing branch, the channeling effect due to rivulet flow is much reduced, therefore, the liquid phase is primarily dispersed as liquid films covering the packing surface. In addition, it is evident to find that $\ln k_G$ is linearly correlated with $\ln S_G$ in the liquid flow rate decreasing branch, whereas in comparison, the relationship is much complicated in the increasing branch. The linear correlation

Table 3. Correlations of the Gas-Phase Relative Permeability Vs. the Gas-Phase Saturation in the Liquid Flow Rate Increasing and Decreasing Branches

		Correlation of the Gas-Phase Permeability	
Packing Size, d_p (mm)	Gas Flow Rate, G (kg m^{-2} s^{-1})	Increasing Branch of the Liquid Flow Rate	Decreasing Branch of the Liquid Flow Rate
1.9	0.065	$k_G = 2.04S_G^{3.25}$	$k_G = 0.90S_G^{2.99}$
	0.130	$k_G = 2.23S_G^{3.45}$	$k_G = 1.01S_G^{3.08}$
	0.195	$k_G = 2.48S_G^{3.84}$	$k_G = 1.05S_G^{3.21}$
3.6	0.065	$k_G = 2.34S_G^{4.91}$	$k_G = 0.87S_G^{4.20}$
	0.130	$k_G = 2.20S_G^{5.23}$	$k_G = 0.95S_G^{4.36}$
	0.195	$k_G = 1.08S_G^{5.73}$	$k_G = 1.08S_G^{4.85}$
5.2	0.065	$k_G = 2.05S_G^{5.21}$	$k_G = 0.88S_G^{4.39}$
	0.130	$k_G = 1.68S_G^{5.35}$	$k_G = 1.00S_G^{4.70}$
	0.195	$k_G = 1.58S_G^{5.82}$	$k_G = 1.06S_G^{5.18}$
9.3	0.065	$k_G = 1.92S_G^{7.80}$	$k_G = 1.86S_G^{7.76}$
	0.130	$k_G = 1.58S_G^{7.12}$	$k_G = 1.27S_G^{6.72}$
	0.195	$k_G = 1.55S_G^{6.96}$	$k_G = 1.05S_G^{6.31}$

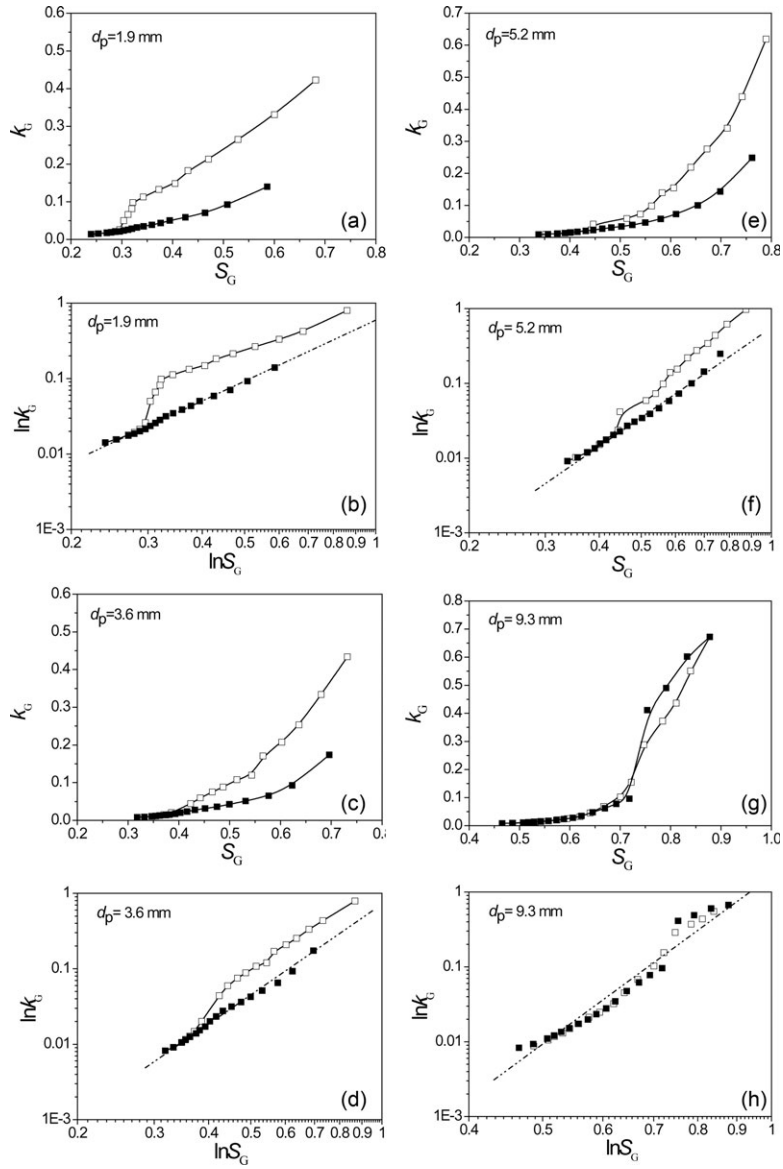

Figure 3. Plot of gas relative permeability against the gas saturation.

□—liquid flow rate increasing; ■—liquid flow rate decreasing. Gas relative permeability plotted on the linear scale for (a) d_p = 1.9 mm, (c) d_p = 3.6 mm, (e) d_p = 5.2 mm, and (g) 9.3 mm. Gas relative permeability plotted on the logarithmic scale for (b) d_p = 1.9 mm, (d) d_p = 3.6 mm, (f) d_p = 5.2 mm, and (h) 9.3 mm.

between lnk_G and lnS_G in the liquid flow rate decreasing branch clearly indicates that there is only one flow pattern, whereas the complicated relationship in the liquid flow rate increasing branch indicates a complex and flow rate dependent liquid flow texture. As in the liquid flow rate decreasing branch, there exists a lower gas phase permeability and a linear correlation between lnk_G and lnS_G, it can be considered that the liquid in this operation mode is in the form of film flow, which is consistent with the view point in the literature.[36,37]

To check the accuracy of pressure drop prediction from the relative permeability correlations given in Table 3, parity plots of pressure drop measurements vs. the predictions are displayed in Figure 4. It shows the majority of the pressure drop data points lies within the ±30% region, and the best agreement is in the case of 1.9-mm packing diameter, whereas the poorest is that of 9.3-mm packing, which means that the 9.3-mm packing is somewhat too large for the two-phase flow pressure drop equation that is situated for small porous media. It should be noted, only the data in the liquid flow rate decreasing branch were compared, in view of its fairly good k_G vs. S_G correlation.

Fraction of Film Flow in the Liquid Texture. In the trickling flow regime, film flow and rivulet flow are in parallel, in this regard, the gas-phase pressure in the film flow region will be equal to that of the trickle bed. As the gas relative permeability k_G in the film flow region can be evaluated from the pressure drop of the trickle bed via Eq. 12, from the correlation between k_G vs. S_G that has been established as a property of film flow, the liquid holdup in the film flow region will be available after the saturation of the gas phase S_G is calculated from Eq. 11.

The fractions of film flow in the liquid texture are shown in Figure 5. As expected, the film flow fraction is almost 100% in the flow rate decreasing branch, whereas it increases from 0 to 100% in the increasing branch. It shows at a specific liquid flow rate, more film flow fraction is

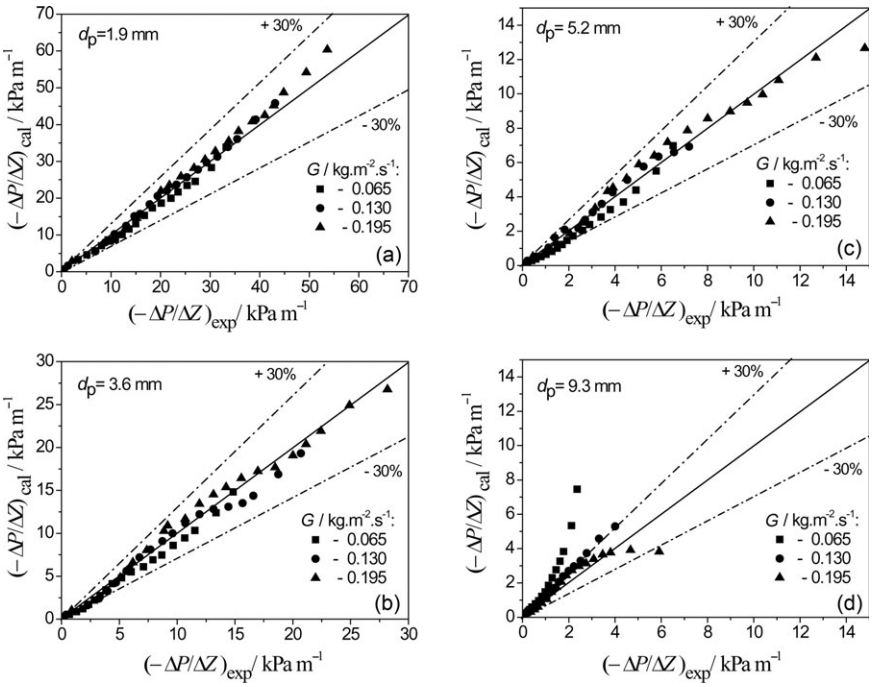

Figure 4. Parity plots of pressure drop measurements vs. the predictions in the liquid flow rate decreasing branch.

Packing diameters of (a) 1.9 mm, (b) 3.6 mm, (c) 5.2 mm, and (d) 9.3 mm.

obtained at a higher gas flow rate, as a result of a stronger gas–liquid interaction, which is beneficial to the generation of film flow. It is also found that the affect of gas flow rate becomes more pronounced when the packing size is increased, for example, it shows that for $d_p = 1.9$ mm there is only a little difference in film flow fraction at different gas flow rates, however, the difference is increased when d_p increases to 3.6 and 5.2 mm, which suggests that the transformation of rivulet flow into film flow requires a smaller gas–liquid interaction for a large particle diameter.

Wetting condition over the bed cross section

A comprehensive wetting condition over the bed cross section can be represented by the fractions of the stagnant liquid, film flow, and rivulet flow regions, which are shown in Figures 6–8.

Rivulet flow was clearly predicted to exist in Figure 6. It shows that the fraction in rivulet flow increases rapidly from 0 to the maximum and then gradually decreases to almost zero in the liquid flow rate increasing direction, whereas in the liquid flow rate decreasing direction, the fraction in

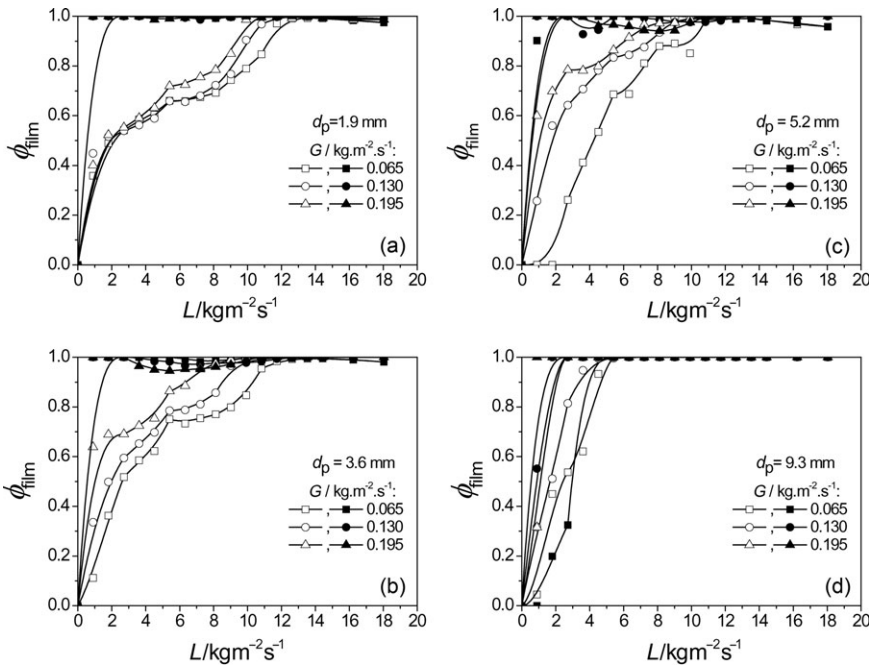

Figure 5. Fractions of film flow in the liquid texture.

○,□,△—liquid flow rate increasing; ●,■,▲—liquid flow rate decreasing. Packing diameters of (a) 1.9 mm, (b) 3.6 mm, (c) 5.2 mm, and (d) 9.3 mm.

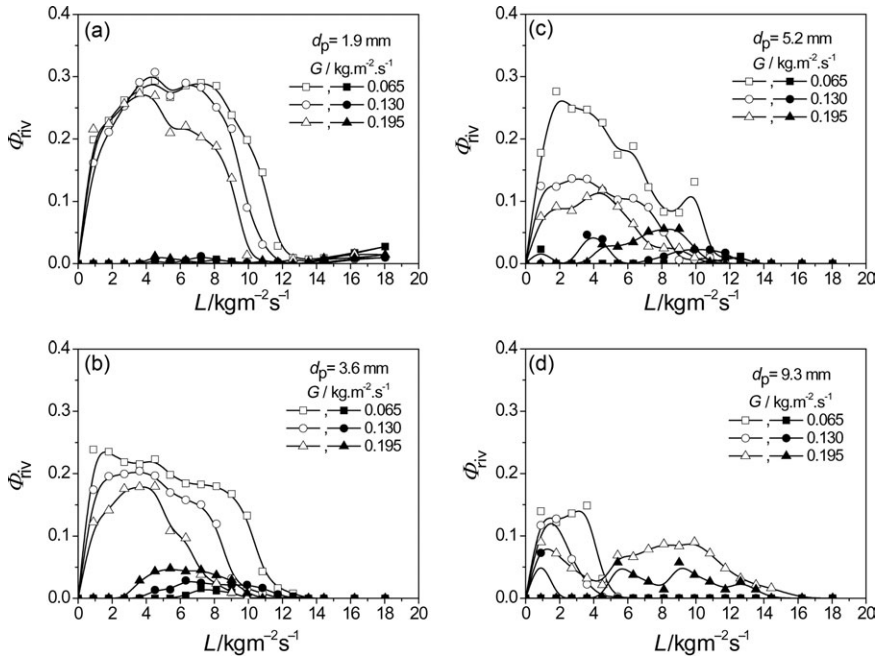

Figure 6. Rivulet flow region fraction over the bed cross section.

○,□,△—liquid flow rate increasing; ●,■,▲—liquid flow rate decreasing. Packing diameters of (a) 1.9 mm, (b) 3.6 mm, (c) 5.2 mm, and (d) 9.3 mm.

rivulet flow is always lower than 5% of the total volume of the reactor for all the four particle diameters. The maximum fraction in rivulet flow is dependent on the packing size and gas flow rate, which is 30% for $d_p = 1.9$ mm, 25–27% for $d_p = 3.6$ and 5.2 mm, and 15% for $d_p = 9.3$ mm. Moreover, it is found that the liquid flow rate interval for rivulet flow is also dependent on the packing size, which decreases from $d_p = 1.9$ to 9.3 mm. The gas flow rate seems to influence the rivulet flow to a large degree, and the fraction of rivulet flow was found largely reduced with the increase of gas flow rate. Besides, the influence of gas flow rate is more obvious with the increase of packing size, for example, in the case of $d_p = 1.9$ mm, the rivulet flow fractions at different gas flow rates are much similar, however, they become much different with larger particle sizes of 3.6 and 5.2 mm.

The packing size effect can be explained from the origin of capillary force, which is inversely proportional to the packing diameter. Therefore, in the case of a small packing

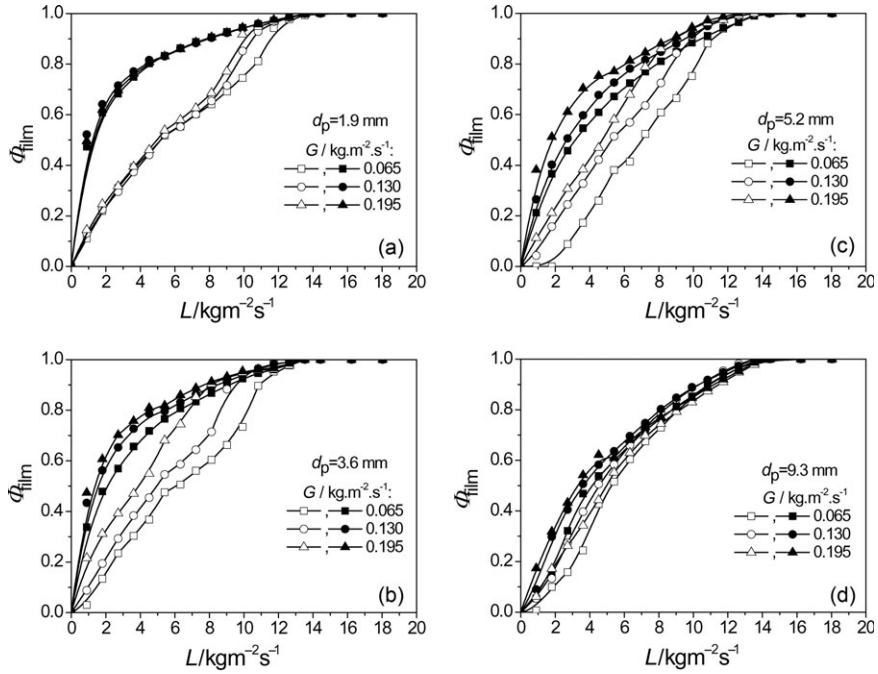

Figure 7. Film flow region fraction over the bed cross section.

○, □, △—liquid flow rate increasing; ●,■,▲—liquid flow rate decreasing. Packing diameters of (a) 1.9 mm, (b) 3.6 mm, (c) 5.2 mm, and (d) 9.3 mm.

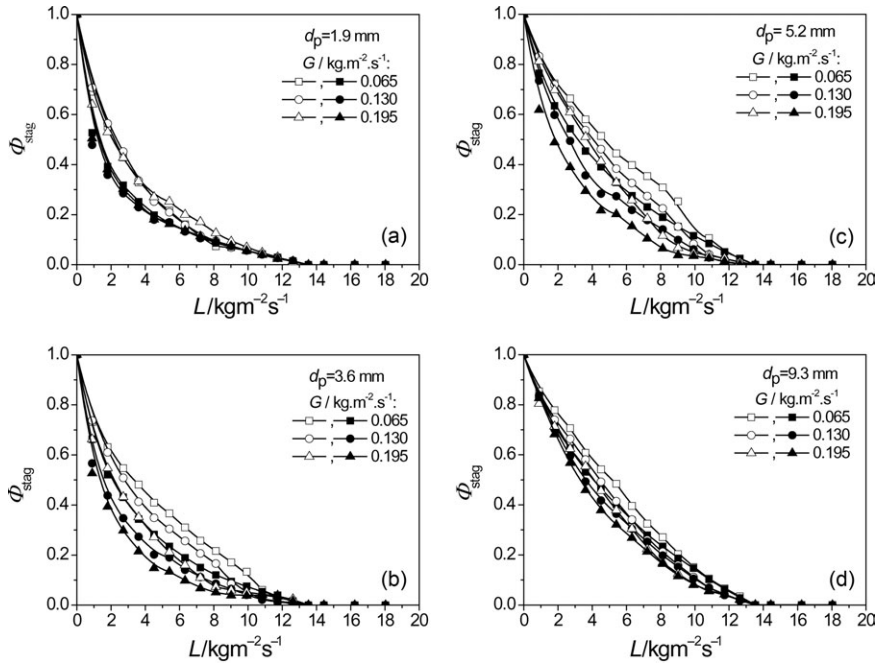

Figure 8. Stagnant liquid region fraction over the bed cross section.

○,□,△—liquid flow rate increasing; ●,■,▲—liquid flow rate decreasing. Packing diameters of (a) 1.9 mm, (b) 3.6 mm, (c) 5.2 mm, and (d) 9.3 mm.

size of 1.9 mm in this work, the rivulet flow will be preferentially developed in the capillary space between particles, and it will not be transformed into film flow, unless the gas–liquid interaction is large enough. Comparatively, in the case of $d_p = 9.3$ mm, we find the rivulet flow is not obvious and not stable, and this result could also be explained from the low capillary effect because of the large packing size. Therefore, the packing size is the most important factor in determining the degree of rivulet flow.

The packing size effect is also observed in the film flow fraction as shown in Figure 7. When the packing diameter was increased from 1.9 to 5.2 mm, the influence of gas flow rate was more and more obvious, and the two branches of film flow fraction approached each other, especially at the highest gas flow rate and the biggest packing diameter. The packing size effect comes to the limit when $d_p = 9.3$ mm, where it shows that the film flow fractions are approximately the same under different gas flow rates, although the film flow fractions

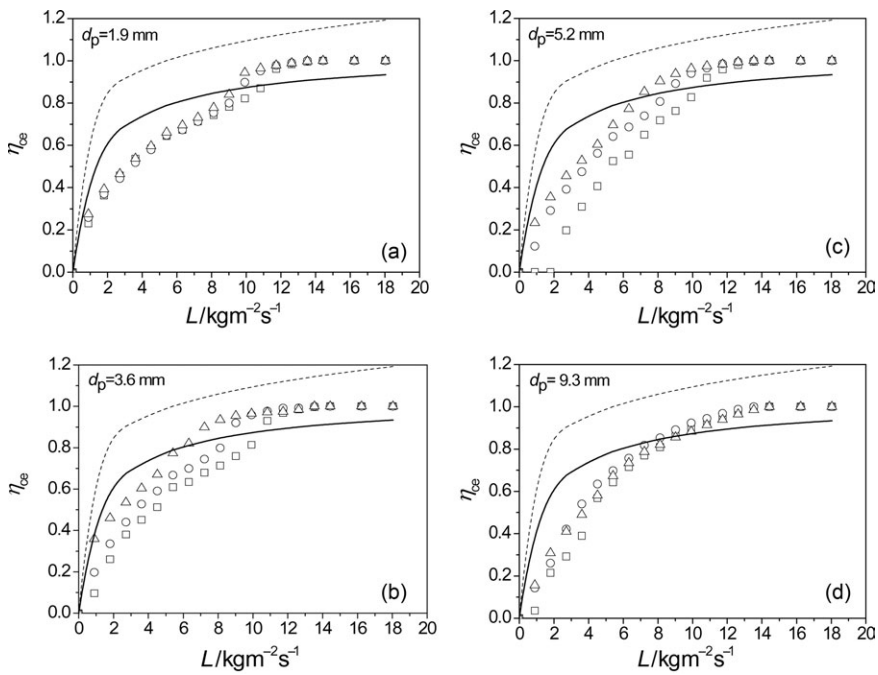

Figure 9. Prediction of liquid–solid wetting efficiency: comparison of Eq. 15 with literature correlations.

Prediction with Eq. 15 at different gas flow rates, G, kg m^{-2} s^{-1}: □—0.065; ○—0.130; △—0.195. Prediction with literature correlations: -----, El-Hisnawi et al.[3]; ——, Mills and Duduković.[4] Packing diameters of (a) 1.9 mm, (b) 3.6 mm, (c) 5.2 mm, and (d) 9.3 mm.

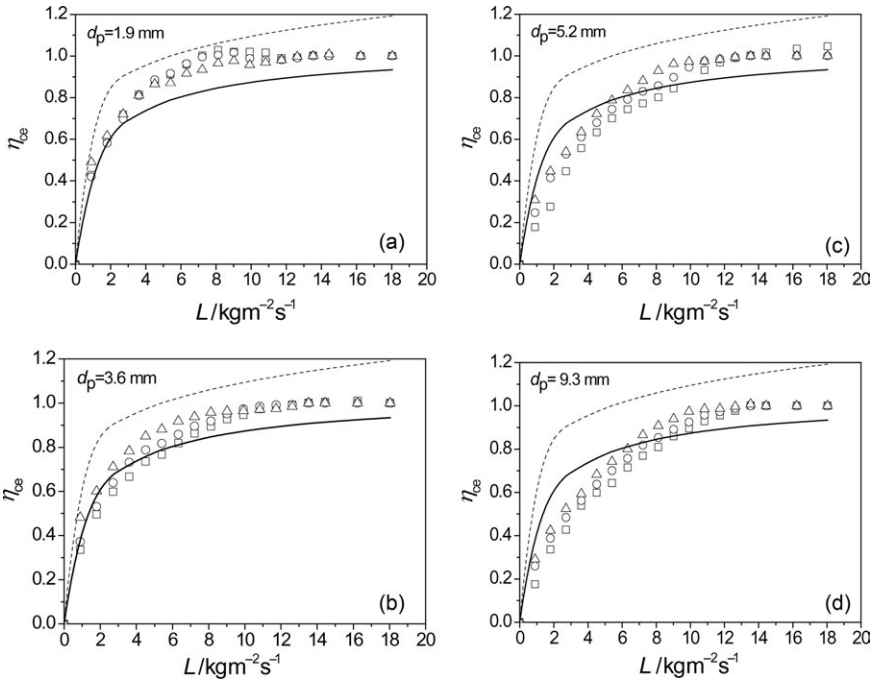

Figure 10. Prediction of liquid–solid wetting efficiency: comparison of Eq. 16 with literature correlations.

Prediction with Eq. 16 at different gas flow rates, G, kg m^{-2} s^{-1}: □—0.065; ○—0.130; △—0.195. Prediction with literature correlations: -----, El-Hisnawi et al.[3]; ——, Mills and Duduković.[4] Packing diameters of (a) 1.9 mm, (b) 3.6 mm, (c) 5.2 mm, and (d) 9.3 mm.

in the liquid flow rate decreasing branch are only a little higher than those in the flow rate increasing branch.

The fractions of stagnant liquid region are plotted in Figure 8 against the liquid flow rate. The figure shows that although the fraction of stagnant liquid region decreases rapidly at a low liquid flow rate, it will not disappear until a large liquid flow rate is reached, therefore, stagnant liquid region will be prevailing in the normal operation regime of a trickle bed.

Evaluation on the liquid–solid external wetting efficiency

As the catalyst packing can only be effectively wetted by the film flow and the rivulet flow of the liquid, the liquid–solid external wetting should be the joint contribution of these two factors. Therefore, external wetting efficiency η_{ce} can be directly written as the total wetting fraction of the packing over the bed cross section

$$\eta_{ce} = \Phi_{film} + \Phi_{riv} \tag{15}$$

To examine the validity of this assumption, the η_{ce} data from Φ_{film} and Φ_{riv} under different operating conditions are calculated according to Eq. 15 and plotted against two frequently used correlations that are proposed by El-Hisnawi et al.[3] and Mills and Duduković,[4] as shown in Figure 9. It shows the experimental data correlated with Eq. 15 are rather scattered, and a poor agreement is observed with the two correlations.

It should be noted that the failure of Eq. 15 may be due to the improper consideration on the contribution of the film flow fraction Φ_{film}. Actually, liquid film provides a surface rather than a volume in the liquid–solid external wetting, while the liquid in rivulet flow is aggregated, whose contribution is equal to its volumetric fraction. Therefore, Eq. 15 should be modified as

$$\eta_{ce} = \Phi_{film}^{\frac{2}{3}} + \Phi_{riv} \tag{16}$$

When the η_{ce} data from Φ_{film} and Φ_{riv} in Eq. 16 are plotted in Figure 10, it shows that much better agreement is obtained with the two correlations.

It should be pointed out that the prediction by Eq. 16 may be more accurate than the two correlations, because it is found in the cases of $d_p = 1.9$ and 3.6 mm, the η_{ce} values predicted by Eq. 16 is in complete agreement with the correlation of Mills and Duduković[4] at low to medium liquid flow rates, however, it lies in the intermediate region between the two correlations at high liquid flow rates. It is conceived from the expression of El-Hisnawi et al.[3] that it would over predict the η_{ce} value at a not too high liquid flow rate, because it would give values exceeding 1.0. On the other hand, the expression of Mills and Duduković[4] is conservative, because η_{ce} value will not reach 1.0 unless the liquid flow rate is infinitely large. Therefore, Eq. 16 compensates for the drawbacks of the two correlations and is more accurate than either of them.

It shows that in Figure 10 the wetting efficiency is decreasing when the packing size is increased from $d_p = 1.9$ to 9.3 mm. However, the good agreement between experiment and correlation in the cases of $d_p = 1.9$ and 3.6 mm does not remain for bigger packing sizes of 5.2 and 9.3 mm. The reason for such a discrepancy is ascribed to the deficiency of the correlation[4] on the packing size effect estimation.

To properly account for the packing size and gas flow rate effects on the liquid–solid wetting efficiency, which have been depicted by the experimental data, a brief correlation based on the Reynolds and Galileo numbers for the two phases is proposed

$$\eta_{ce} = 4.85 Re_L^{0.42} Ga_L^{-0.25} Re_G^{0.083} \tag{17}$$

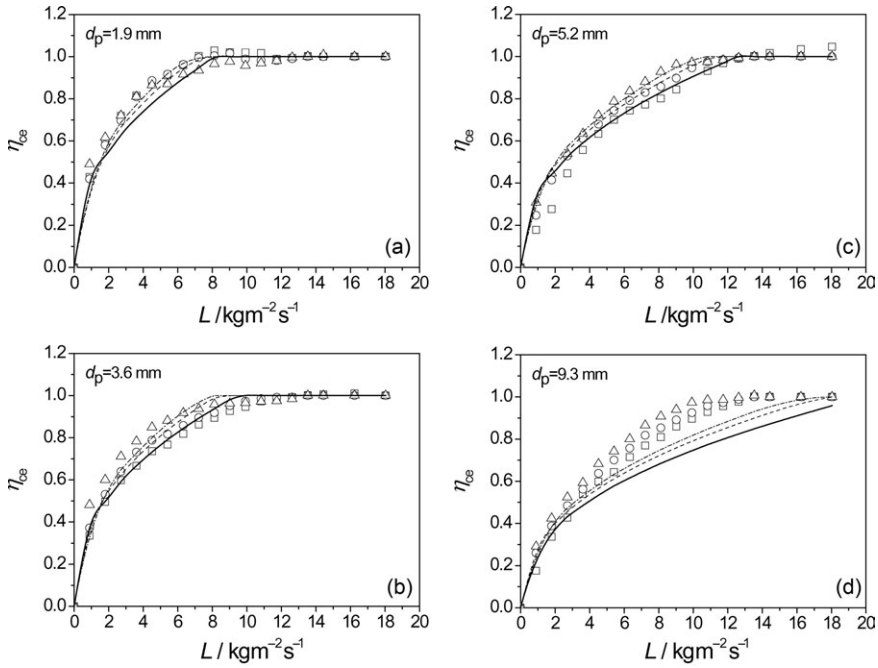

Figure 11. Prediction of liquid–solid wetting efficiency: comparison of experimental data with new correlation Eq. 17.

Gas flow rates (kg m^{-2} s^{-1}): experimental data: □—0.065; ○—0.130; △—0.195 and prediction: ——, 0.065; -----, 0.130; - - -, 0.195. Packing diameters of (a) 1.9 mm, (b) 3.6 mm, (c) 5.2 mm, and (d) 9.3 mm.

It shows from Figure 11 that fairly good agreement has been obtained for packing diameters from 1.9 to 5.2 mm between the prediction by Eq. 17 and experimental data, which suggests that Eq. 17 can be reliably used in the estimation of external wetting efficiency of a catalytic bed.

It should be noted that in Eq. 17 the influence of liquid flow rate was found to a power of 0.42, which seems to be much higher than some literature reports of 0.146[3], 0.222[40], 0.25–0.4,[41] and so forth. However, it is a reasonable value, because according to Roberts and Yadwadkar,[42] who found that the external wetting efficiency of a plate with a liquid flow could be correlated by

$$\eta_{ce} = aL^{\frac{3s-1}{2}} \tag{18}$$

where L is liquid flow rate, and s is normally between 0.5 and 0.75. Therefore, η_{ce} is proportional to 0.25–0.63 power of the liquid flow rate, which means that the power 0.42 obtained in this work lies in the middle of this region.

Conclusions

In this work, a fluid dynamically based mathematical method for evaluation of liquid–solid contacting efficiency was proposed as a new attempt. The accomplishment of this investigation is based on the knowledge of several important concepts, which are specific to a trickling flow reactor, associated with the liquid flow texture, the operation-history depended hysteresis behavior, as well as the consistent correlation between permeability and gas saturation. Some critical points have been derived from the development of this work:

1. An excellent linear relationship on a logarithmic coordination system has been observed between the relative permeability and the gas saturation in the liquid flow rate decreasing operation, which means that in this operation mode the fluid flow texture is kept constant and can be viewed as film flow, whereas the nonlinear relationship observed in the liquid flow rate increasing operation means a continually changed flow texture, which varies from a mixture of rivulet flow and film flow to complete film flow.

2. Packing size is the most significant factor to the formation of rivulet flow. As rivulet flow refers to the liquid channeling between the packings, the capillary force exerted to keep the rivulet flow will be more significant in the case of small particles than in the larger ones, therefore, the transformation of rivulet flow into film flow requires a larger gas–liquid interaction.

3. It is important to discriminate the liquid flow texture into different components, because they are contributing to the external liquid–solid wetting efficiency in different ways. The liquid film is to provide liquid–solid contacting area, whereas the rivulet is to provide liquid–solid contacting volume, therefore, the external wetting efficiency should be the total contribution of the two-third power of the liquid film fraction plus the rivulet flow fraction.

Acknowledgments

The authors are grateful to the financial supports of Natural Science Foundation of China (20876043 and 21076072) and Fundamental Research Funds for the Central Universities of China.

Notation

A, B = Ergun equation coefficients, defined in Eq. 5
d_p = packing diameter, m
Eö = Eötvos number, defined in Eq. 14
g = gravitational acceleration, m s^{-2}
G = gas flow rate, kg m^{-2} s^{-1}
Ga = Galileo number, $\rho^2 g d_p^3/\mu^2$
Ga* = modified Galileo number, $\rho^2 g d_p^3 \varepsilon_b^3/\mu^2(1-\varepsilon_b)^3$
k = relative permeability
L = liquid flow rate, kg m^{-2} s^{-1}
P = pressure, N m^{-2}
Re = Reynolds number, $\rho u d_p/\mu$
Re* = modified Reynolds number, $\rho u d_p/\mu(1-\varepsilon_b)$
s = parameter in Eq. 18

u = superficial velocity, m s^{-1}
Z = axial distance, m

Greek letters

α = coefficient in Eq. 11
β = exponent in Eq. 11
ε = porosity or holdup
ρ = density, kg m^{-3}
σ = surface tension, N m^{-1}
ϕ = volumetric fraction, defined in Figure 5
Φ = volumetric fraction, defined in Eq. 1
η = wetting efficiency
μ = viscosity, Pa s
ψ = Dimensionless pressure drop, defined in Eq. 6

Subscripts

b = the bed averaged
ce = contacting efficiency
p = packing
L = dynamic liquid
G = gas phase
film = film flow
riv = rivulet flow
s = static liquid
stag = stagnant liquid

Literature Cited

1. Schwartz JG, Weger E, Duduković MP. A new tracer method for determination of liquid–solid contacting efficiency in trickle bed reactors, *AIChE J*. 1976;22:894–904.
2. Colombo AJ, Baldi G, Sicardi S. Solid–liquid contacting effectiveness in trickle bed reactors. *Chem Eng Sci*. 1976;31:1101–1108.
3. El-Hisnawi AA, Duduković MP, Mills PL. Trickle-bed reactors: dynamic tracer tests, reaction studies, and modeling of reactor performance. *ACS Symp Ser*. 1981;196:421–440.
4. Mills PL, Duduković MP. Evaluation of liquid–solid contacting in trickle-bed reactors by tracer methods. *AIChE J*. 1981;27:893–904.
5. Ring ZE, Missen RW. Trickle-bed reactors: tracer study of liquid holdup and wetting efficiency at high temperature and pressure. *Can J Chem Eng*. 1991;69:1016–1020.
6. Julcour-Lebigue C, Baussaron L, Delmas H, Wilhelm AM. Theoretical analysis of tracer method for the measurement of wetting efficiency. *Chem Eng Sci*. 2007;62:5374–5379.
7. Herskowitz M, Carbonell RG, Smith JM. Effectiveness factors and mass transfer in trickle bed reactors. *AIChE J*. 1979;25:272–283.
8. Llano JJ, Rosal R, Sastre H, Diez FV. Determination of wetting efficiency in trickle-bed reactors by a reaction method. *Ind Eng Chem Res*. 1997;36:2616–2625.
9. Pironti F, Mizrahi D, Acosta A, Gonzalez-Mendizabal D. Liquid–solid wetting factor in trickle bed reactors: its determination by a physical method. *Chem Eng Sci*. 1999;54:3793–3800.
10. Al-Dahhan MH, Duduković MP. Catalyst wetting efficiency in trickle-bed reactors at high pressure. *Chem Eng Sci*. 1995;50:2377–2389.
11. Hofmann, HP. Multiphase catalytic packed-bed reactors. *Catal Rev Sci Eng*. 1978;17:71–117.
12. Ng KM, Chu CF. Trickle-bed reactors. *Chem Eng Progr*. 1987;83:55–63.
13. Lutran PG, Ng KM, Delikat EP. Liquid distribution in trickle beds. An experimental study using computer-assisted tomography. *Ind Eng Chem Res*. 1991;30:1270–1280.
14. Sederman AJ, Gladden LF. Magnetic resonance imaging as a quantitative probe of gas–liquid distribution and wetting efficiency in trickle-bed reactors. *Chem Eng Sci*. 2001;56:2615–2628.
15. Van der Merwe W, Nicol W, de Beer F. Three-dimensional analysis of trickle flow hydrodynamics: computed tomography image acquisition and processing. *Chem Eng Sci*. 2007;62:7233–7244.
16. Marchot P, Toye D, Pelsser AM, Crine M, L'Homme G, Olujic Z. Liquid distribution images on structured packing by X-ray computed tomography. *AIChE J*. 2001;47:1471–1476.
17. Toye D, Marchot P, Crine M, Pelsser AM, L'Homme G. Local measurements of void fraction and liquid holdup in packed columns using X-ray computed tomography. *Chem Eng Process*. 1998;37:511–520.
18. Van der Merwe W, Nicol W, De Beer F. Trickle flow distribution and stability by X-ray radiography. *Chem Eng J*. 2007;132:47–59.
19. Kumar SB, Moslemian D, Duduković MP. A γ-ray tomographic scanner for imaging voidage distribution in two-phase flow systems. *Flow Measure Instrum*. 1995;6:61–73.
20. Boyer C, Fanget B. Measurement of liquid flow distribution in trickle bed reactor of large diameter with a new gamma-ray tomographic system. *Chem Eng Sci*. 2002;57:1079–1089.
21. Ravindra PV. Rao DP, Rao MS. Liquid flow texture in trickle bed reactors: an experimental study. *Ind Eng Chem Res*. 1997;36:5133–5145.
22. Baussaron L, Julcour-Lebigue C, Wilhelm AM, Boyer C, Delmas H. Partial wetting in trickle bed reactors: measurement techniques and global wetting efficiency. *Ind Eng Chem Res*. 2007;46:8397–8405.
23. Baussaron L, Julcour-Lebigue C, Wilhelm AM, Delmas H, Boyer C. Wetting topology in trickle bed reactors. *AIChE J*. 2007;53:1850–1860.
24. Jiang Y, Khadilkar MR, Al-Dahhan MH, Duduković MP. CFD of multiphase flow in packed-bed reactors: II. Results and applications. *AIChE J*. 2002;48:716–730.
25. Lopes RJG, Quinta-Ferreira RM. Three-dimensional numerical simulation of pressure drop and liquid holdup for high-pressure trickle-bed reactor, *Chem Eng J*. 2008;145:112–120.
26. Lopes RJG, Quinta-Ferreira RM. CFD modelling of multiphase flow distribution in trickle beds. *Chem Eng J*. 2009;147:342–355.
27. Lopes RJG, Quinta-Ferreira RM. Assessment of CFD Euler–Euler method for trickle-bed reactor modelling in the catalytic wet oxidation of phenolic wastewaters. *Chem Eng J*. 2010;160:293–301.
28. Atta A, Roy S, Nigam KDP. Prediction of pressure drop and liquid holdup in trickle bed reactor using relative permeability concept in CFD. *Chem Eng Sci*. 2007;62:5870–5879
29. Atta A, Roy S, Nigam KDP. A two-phase Eulerian approach using relative permeability concept for modeling of hydrodynamics in trickle-bed reactors at elevated pressure. *Chem Eng Res Des*. 2010;88:369–378.
30. Lopes RJG, Quinta-Ferreira RM. Volume-of-fluid-based model for multiphase flow in high-pressure trickle-bed reactor: optimization of numerical parameters. *AIChE J*. 2009;55:2920–2933.
31. Lopes RJG, de Sousa VSL, Quinta-Ferreira RM. CFD and experimental studies of reactive pulsing flow in environmentally-based trickle-bed reactors. *Chem Eng Sci*. 2011;66:3280–3290.
32. Nemec D, Levec J. Flow through packed bed reactors: 2. Two-phase concurrent downflow. *Chem Eng Sci*. 2005:60;6958–6970.
33. Crine M, Marchot P, L'Homme G. Statistical hydrodynamics in trickle flow columns. *AIChE J*. 1992;38:136–147.
34. Wang R, Mao Z, Chen J. Experimental and theoretical studies of pressure drop hysteresis in trickle bed reactors. *Chem Eng Sci*. 1995;50:2321–2328.
35. Specchia V, Baldi G. Pressure drop and liquid hold-up for two-phase co-current flow in packed beds. *Chem Eng Sci*. 1977;32:515–523.
36. Levec J, Grosser, K, Carbonell, R.G. The hysteretic behavior of pressure drop and liquid holdup in trickle beds. *AIChE J*. 1988;34:1027–1030.
37. Christensen G, McGovern S J, Sundaresan S. Cocurrent downflow of air and water in a two-dimensional packed column. *AIChE J*. 1986;32:1677–1689.
38. Sáez AE, Carbonell RG. Hydrodynamic parameters for gas–liquid cocurrent flow in packed beds. *AIChE J*. 1985;31:52–62.
39. Lakota A, Levec J, Carbonell RG. Hydrodynamics of trickling flow in packed beds: relative permeability concept. *AIChE J*. 2002;48:731–738.
40. Burghardt A, Bartelmus G, Jaroszynski M, Kolodziej A. Hydrodynamics and mass transfer in a three-phase fixed-bed reactor with cocurrent gas–liquid downflow. *Chem Eng J*. 1995;58(2):83–99.
41. Satterfield CN. Trickle-bed reactors. *AIChE J*. 1975;21:209–228.
42. Roberts GW, Yadwadkar SR. The efficiency of liquid–solid contacting in trickle-bed reactors. In: National AIChE Meeting, Dalas, TX, February 1972.

Manuscript received Dec. 4, 2011, and revision received Feb. 7, 2012.